

# Activation of Silicon Implanted with Phosphorus and Boron Atoms by Infrared Semiconductor Laser Rapid Annealing

Kan Ukawa<sup>1</sup>, Yasushi Kanda<sup>1</sup>, Toshiyuki Sameshima<sup>1\*</sup>, Naoki Sano<sup>2</sup>, Masao Naito<sup>3</sup>, and Nariaki Hamamoto<sup>3</sup>

<sup>1</sup> Tokyo University of Agriculture and Technology, Koganei, Tokyo 184-8588, Japan

<sup>2</sup> Hightec Systems Corporation, Yokohama 222-0033, Japan

<sup>3</sup> Nissin Ion Equipment Co., Ltd., Koka, Shiga 528-0068, Japan

Received February 9, 2010; accepted April 21, 2010; published online July 20, 2010

We report the activation of silicon implanted with phosphorus and boron atoms by infrared semiconductor laser annealing using carbon films as an optical absorption layer. 2- $\mu\text{m}$  surface region was heated above 1000 °C longer than 22  $\mu\text{s}$  by scanning the laser beam for a dwell time of 40  $\mu\text{s}$ . We carried out implantations of  $1 \times 10^{15} \text{ cm}^{-2}$  phosphorus atoms at 100, 300, and 500 keV, and boron clusters with a boron concentration of  $1 \times 10^{15} \text{ cm}^{-2}$  at 6 keV. Laser irradiation at 375 kW/cm<sup>2</sup> was conducted to activate impurities. Secondary ion mass spectrometry measurement revealed that laser annealing caused no substantial change in the phosphorus and boron atom profiles. Laser-induced recrystallization of surface amorphized regions caused by the ion implantation was analyzed using the optical reflectivity spectra ranging from 250 to 1000 nm. The free carrier absorption analyses indicated that the phosphorus and boron atoms were effectively activated by laser annealing.

© 2010 The Japan Society of Applied Physics

DOI: 10.1143/JJAP.49.076503

## 1. Introduction

Laser rapid heating is attractive for activating semiconductor materials implanted with impurity atoms, which is a fundamental process in order to fabricate semiconductor devices. A high activation ratio and no serious impurity diffusion are required to fabricate an extremely shallow source/drain extension (SDE) region with a depth of 10 nm order in metal–oxide–semiconductor (MOS) transistor devices for the 45 nm node and below, which cannot be achieved by conventional rapid thermal annealing (RTA).<sup>1–4</sup> Activation of impurity atoms in deep silicon region is also important to fabricate devices such as insulated gate bipolar transistors (IGBTs). A method of excimer laser annealing for about 10<sup>−9</sup> s has been developed for this purpose.<sup>2–4</sup> We have investigated continuous wave (CW) infrared semiconductor laser annealing using a carbon layer as an optical absorption layer.<sup>5–7</sup> The infrared semiconductor laser is attractive to heating processes with high throughput because of its high power of ~10 kW, its high conversion efficiency of ~50% and its stable emission. In order to solve the problem of the low optical absorbance of Si in the infrared region, we used carbon as a photo absorption layer. A black carbon layer with a high heat resistivity of ~5000 K can serve as a heat source at high temperatures.<sup>8</sup> It also has a high optical absorbance in the infrared region because of its high extinction coefficient and low refractive index giving a low reflection loss. A carbon optical absorption layer also plays a role in reducing the unexpected modulation of light intensity due to the Fresnel optical diffraction effect caused by surface texture during the fabrication of transistor devices.

In this paper, we report the activation of silicon implanted with phosphorus and boron atoms using rapid CW infrared semiconductor laser annealing from 15 to 43  $\mu\text{s}$ . First of all, we demonstrate the rapid heating properties of silicon surface regions by numerical heat flow simulation in order to determine the laser irradiation conditions of rapid heating at high temperatures. Next, we report the recrystallization properties of the disordered amorphous regions formed by phosphorus implantation. We then report the activation of

phosphorus atoms. We discuss in detail the activation behavior in the case of phosphorus atoms distributing to 2  $\mu\text{m}$  deep from the surface using the free carrier optical absorption theory. We then show the electrical current characteristics of N<sup>+</sup>P diodes formed in laser induced activated regions. Finally, we report the activation of silicon implanted with boron atoms located within 10 nm from surface.

## 2. Experimental Procedure

Ion implantation of phosphorus atoms with a concentration of  $1 \times 10^{15} \text{ cm}^{-2}$  was conducted for p-type silicon substrates with a resistivity of 10  $\Omega \text{ cm}$ . The acceleration energies were 100, 300, and 500 keV. Ion implantation of boron clusters was also carried out at 6 keV with a boron concentration of  $1 \times 10^{15} \text{ cm}^{-2}$  for shallow doping. Black carbon films with a thickness of 200 nm were formed on the silicon surface by sputtering. Optical measurements revealed that the optical absorbance was 75% at 976 nm, which was the wavelength of our laser light. Figure 1 shows the CW infrared semiconductor laser annealing system with a beam scanning mechanism. The laser beam was introduced by an optical fiber to optics, which focus the laser to a width of 500  $\mu\text{m}$  and a length of 15  $\mu\text{m}$  at the surface of the samples. When the laser power was 40 W, the peak power intensity was 500 kW/cm<sup>2</sup> at the surface of samples. The effective heating power intensity was 375 kW/cm<sup>2</sup> because of reflection loss. Samples were mounted on an X–Y movable stage driven by linear motors at a velocity from 35 to 100 cm/s in the Y-direction during laser irradiation. The effective laser dwell time was given by the beam length of 15  $\mu\text{m}$  divided by the laser beam scanning velocity. It ranged from 15 to 43  $\mu\text{s}$ . The stage was also moved with a 250  $\mu\text{m}$  step in the X-direction. After laser irradiation, the carbon layer was removed by oxygen plasma treatment. We also carried out laser irradiation without carbon layer formation for comparison.

A numerical heat flow simulation was carried out to estimate the temperature increase on the silicon surface using a numerical analysis program constructed with the two-dimensional finite element method. Secondary ion mass spectroscopy (SIMS) analysis was conducted to measure the in-depth profiles of phosphorus and boron concentrations. Optical reflectivity spectra ranging from 250 to 1000 nm

\*E-mail address: tsamesim@cc.tuat.ac.jp

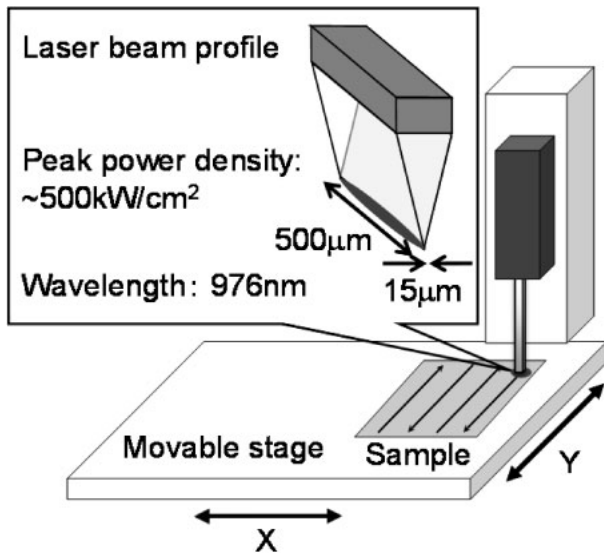


Fig. 1. CW infrared semiconductor laser annealing system with a beam scanning mechanism.

were measured using a conventional spectrometer to investigate the crystalline state at the surface region in order to analyze the in-depth distribution of crystalline volume ratio by a numerical calculation program using the Fresnel optical interference effect.<sup>5)</sup> The rear surfaces of the samples were polished for the measurement of infrared transmissivity spectra by Fourier transform infrared (FTIR) spectrometry. Experimental infrared transmissivity spectra were analyzed to estimate the carrier density in-depth profiles, carrier mobility, and sheet resistance by a numerical program using free carrier absorption and optical interference theories.<sup>9,10)</sup> Diodes with a mesa structure were fabricated to evaluate the electrical properties of the pn junction.

### 3. Results and Discussion

#### 3.1 Calculation of rapid heating

We calculated the change in temperature to estimate the rapid heating of silicon by scanning the laser beam. A two-dimensional finite element heat flow simulation program was developed to investigate the change in temperature at the silicon surface caused by a Gaussian-type heat source at 375 kW/cm<sup>2</sup> with a width of 20 μm moving on the surface at velocities from 0.5 to 2 m/s. Figure 2(a) shows calculated changes in temperature at a point on the silicon surface with time when the moving heat source arrived at the calculation point at 0 s and pass through it after different dwell times of 10, 20, 30, and 40 μs. The calculation point was heated to 480 °C for a dwell time of 40 μs just at heat source reaching because of substantial heat diffusion in the lateral direction of heat source moving. The temperature increased to the maximums of 550, 820, 1040, and 1390 °C for the dwell times of 10, 20, 30, and 40 μs, respectively. Figure 2(b) shows the temperatures at different depths ranging from 0 to 2.0 μm for the laser dwell time of 40 μs as a function of time. The top 2 μm surface region was uniformly heated to 480 °C when the moving heat source arrived at the calculation point at 0 s because of lateral heat diffusion. On the other hand, the maximum temperature decreased from 1390 to 1130 °C as the depth increased from 0 to 2.0 μm because of effective

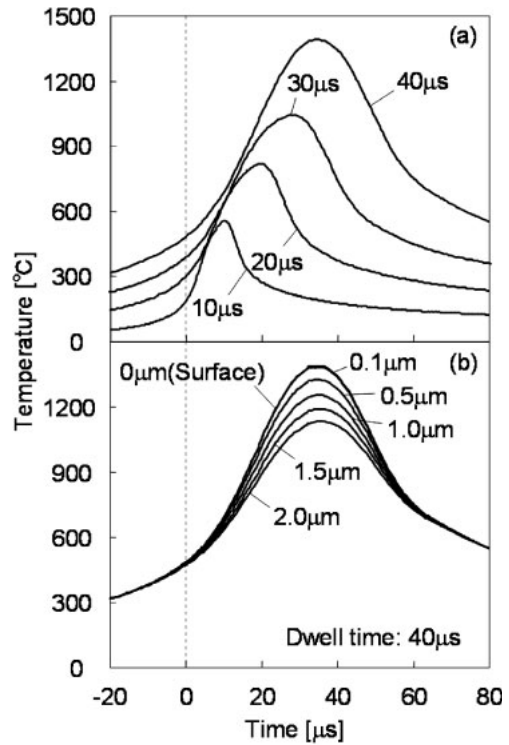


Fig. 2. Calculated changes in temperature at a point on the silicon surface for the laser dwell times of 10, 20, 30, and 40 μs (a) as well as at different depths ranging from 0 to 2.0 μm for the laser dwell time of 40 μs (b) as a function of time.

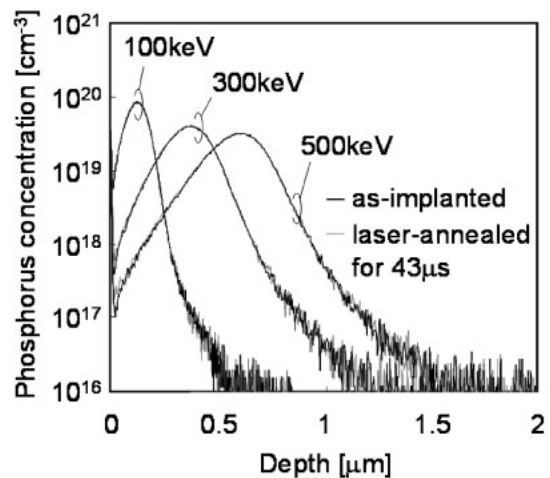
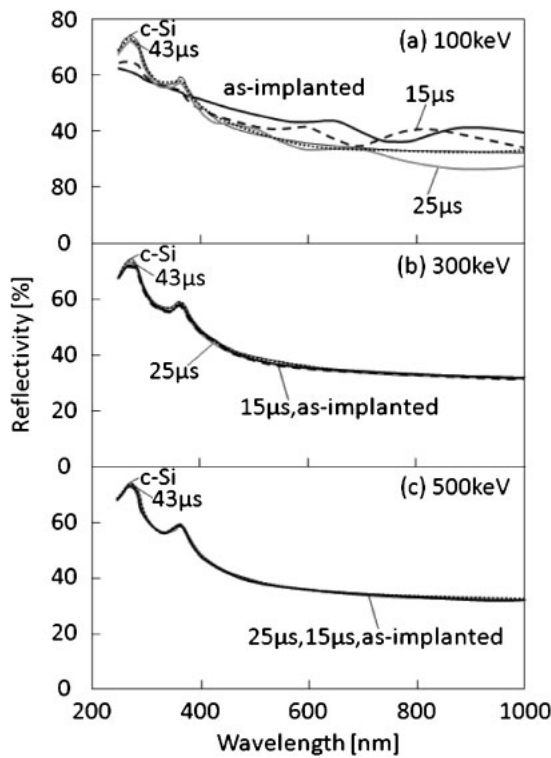


Fig. 3. Phosphorus concentration in-depth profiles for as-implanted and laser-annealed samples for a dwell time of 43 μs in the cases of implantations with a concentration of  $1 \times 10^{15} \text{ cm}^{-2}$  at 100, 300, and 500 keV.

heating of the top surface by the heat source. The top 2 μm surface region was heated above 1000 °C for longer than 22 μs. The temperature rapidly decreased to 500 °C at 80 μs at each depth because of heat diffusion in the depth and lateral directions in silicon.

#### 3.2 Phosphorus doping

Figure 3 shows the phosphorus concentration in-depth profiles for samples as-implanted and laser-annealed for a dwell time of 43 μs in the cases of implantations at 100, 300, and 500 keV. The depths of the peak phosphorus concen-



**Fig. 4.** Optical reflectivity spectra for samples as-implanted and laser-annealed for the dwell times of 15–43 μs in the cases of phosphorus implantations at  $1 \times 10^{15} \text{ cm}^{-2}$  at 100 (a), 300 (b), and 500 keV (c).

tration were 0.13, 0.37, and 0.62 μm for ion implantations at 100, 300, and 500 keV, respectively. The phosphorus atoms reached 2 μm deep in the case of 500 keV implantation. There was no substantial change in the phosphorus concentration profiles caused by 43-μs laser annealing in each implantation case. These results reveal that the heating duration was sufficiently short for phosphorus atoms to maintain their initial profiles. SIMS measurement also revealed that the effective dose of phosphorus atoms for implantations at 100, 300, and 500 keV was  $1.0 \times 10^{15} \text{ cm}^{-2}$  for all the as-implanted and laser-annealed samples.

Figure 4 shows optical reflectivity spectra for as-implanted and laser-annealed samples for dwell times from 15 to 43 μs in the cases of phosphorus implantations at  $1 \times 10^{15} \text{ cm}^{-2}$  at 100 (a), 300 (b), and 500 keV (c). There were no  $E_1$  and  $E_2$  peaks in the ultraviolet region for the as-implanted sample in the case of implantation at 100 keV. This means that the surface region was amorphized by the phosphorus implantation at 100 keV. Peaks at 650 and 920 nm and a valley at 770 nm were observed in the spectrum from as-implanted sample. The oscillating line shape results from an optical interference effect in the layered structure of air/amorphized layer/crystalline silicon. A small  $E_2$  peak appeared at approximately 280 nm in the spectrum laser-annealed for 15 μs. The oscillating line shape was also changed by the laser annealing in visible and infrared wavelength regions. This means that the 15-μs laser annealing caused recrystallization of the silicon surface region. Although the  $E_1$  and  $E_2$  peaks increased to almost the same height as that of single crystalline silicon as the dwell time increased to 25 μs, peaks at 500 and 700 nm and valleys at 600 and 870 nm were still observed in the reflectivity

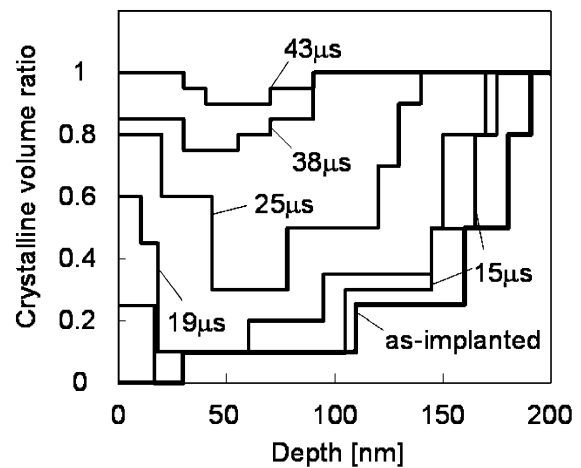


**Fig. 5.** In-depth distribution of the crystalline volume ratio analyzed using the optical reflectivity spectra shown in Fig. 4(a) in the case of phosphorus implantation at 100 keV.

spectra. The large  $E_1$  and  $E_2$  peaks indicate that the surface region was well recrystallized by 25-μs laser annealing because of the high absorption coefficient in the ultraviolet region. The oscillating reflectivity spectra in the visible and infrared regions indicate a buried amorphized region below the surface. The spectral oscillation in the visible and infrared wavelength regions was finally removed by laser annealing for 43 μs.

On the other hand, the spectra for the as-implanted samples in the cases of 300 and 500 keV were almost the same as that of single crystalline silicon, as shown in Figs. 4(b) and 4(c). These results indicate that the surface regions almost maintain their crystalline states in the cases of phosphorus implantations at 300 and 500 keV. The spectra for the laser-annealed samples were also almost the same as that of crystalline silicon.

The in-depth distribution of the crystalline volume ratio was investigated in the case of phosphorus implantation at 100 keV for as implanted as well as laser-annealed samples with different laser dwell times, by analysis of the optical reflectivity spectra given in Fig. 4(a) using our numerical analysis program, as shown in Fig. 5.<sup>5)</sup> The top 30 nm region was completely amorphized, and the underlying region was partially amorphized to a depth of 190 nm by the phosphorus implantation at 100 keV. 15-μs laser annealing caused slight recrystallization in the top 17 nm region. The crystalline volume ratio also increased in the deep region. The crystalline volume ratio particularly increased in the surface region and in the deep region as the dwell time increased. For 43-μs laser annealing, the top 30 nm region was completely crystallized, and there was a partially amorphized region between the depths of 30 and 90 nm. This result means that there are two types of recrystallization. One is recrystallization that proceeded from the deep region to the surface region. The other is recrystallization that occurred at the surface region. Bulk crystalline in the deep region can play the role of nucleation sites for the recrystallization that proceeded from the deep region. Crystallization in the random nucleation mode probably occurred in the surface region, because the crystalline nucleation density can be high when sample is heated to a high temperature.<sup>11)</sup>

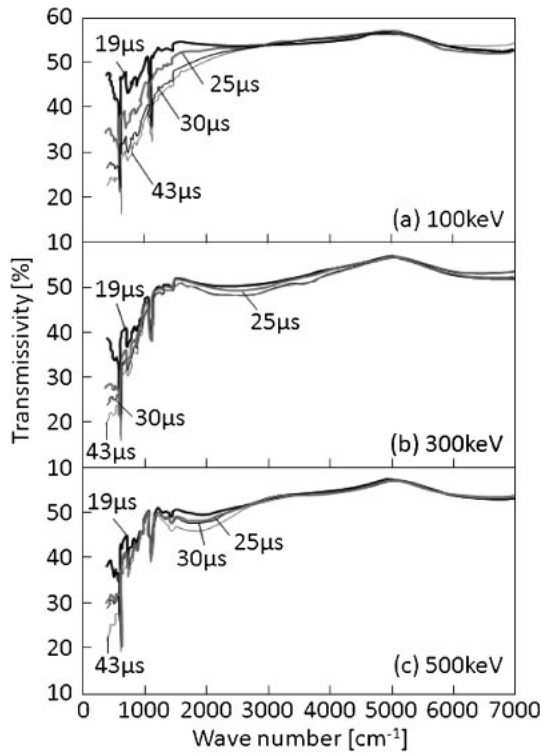


**Fig. 6.** Transmissivity spectra for samples annealed for dwell times from 19 to 43  $\mu\text{s}$  for phosphorus implantation at 100 (a), 300 (b), and 500 keV (c).

Figure 6 shows transmissivity spectra for samples annealed for dwell times from 19 to 43  $\mu\text{s}$  for phosphorus implantation at 100 (a), 300 (b), and 500 keV (c). A decrease in transmissivity was observed in every spectrum for wave numbers below 1000  $\text{cm}^{-1}$  owing to the substantial free carrier optical absorption, particularly in the case of the long laser dwell time. Figure 7 shows the difference in transmissivity spectra calculated by subtracting the transmissivity spectra shown in Fig. 6 from the spectrum of undoped silicon in the cases of phosphorus implantations at 100 (a), 300 (b), and 500 keV (c). Figure 7(a') shows a 2.5 time magnification in vertical axis of Fig. 7(a). The difference in the transmissivity below 3000  $\text{cm}^{-1}$  increased for the case of phosphorus implantation at 100 keV as the laser dwell time increased owing to the substantial free carrier optical absorption, as shown in Fig. 7(a). A weak valley at 2900  $\text{cm}^{-1}$  was observed in the spectrum for the dwell time of 19  $\mu\text{s}$ . The valley shifted to higher wave number as the dwell time increased, as shown by lines in Fig. 7(a'). This shift means that the free carrier region expanded to the surface region as the dwell time increased.<sup>12)</sup> In the case of phosphorus implantation at 300 keV, valleys at 1500 and 5000  $\text{cm}^{-1}$  as well as a peak at 2600  $\text{cm}^{-1}$  were observed in every spectrum, as shown in Fig. 7(b). Moreover, valleys at 1000, 3000, and 5000  $\text{cm}^{-1}$  as well as peaks at 1800 and 4300  $\text{cm}^{-1}$  were observed in every spectrum for the case of 500 keV implantation, as shown in Fig. 7(c). The wave numbers of those valleys and peaks did not change even as the laser dwell time increased. The peak heights at 2600 and 1800  $\text{cm}^{-1}$  for phosphorus implantations at 300 and 500 keV, respectively, increased as the laser dwell time increased. This means that the carrier density increased as the laser dwell time increased.

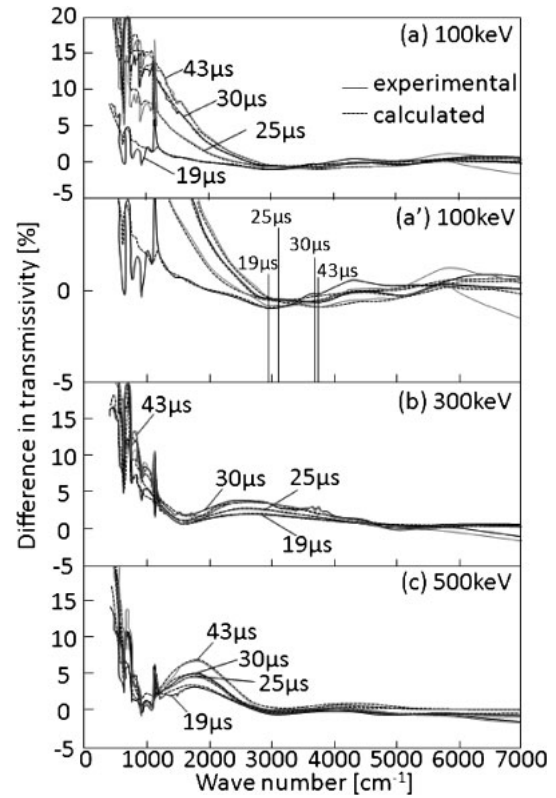


**Fig. 7.** Difference in transmissivity spectra calculated by subtracting the transmissivity spectra shown in Fig. 6 from the spectrum of undoped silicon in the cases of phosphorus implantations at 100 (a), 2.5 times magnification in vertical axis of (a,a'), 300 (b), and 500 keV (c). The valley positions of the spectra are indicated by lines in (a'). The calculated spectra were also represented in (a)–(d).

We analyzed the experimental spectra shown in Fig. 7 using our numerical calculation program in order to estimate free carrier density distributions. The free carrier absorption effect is explained by Drude theory. The free carriers vibrate owing to the electrical field of the infrared light in silicon. The vibration of free carriers causes polarization, which induces a change in the effective dielectric constant. The real part of the complex dielectric constant  $\epsilon_r$  and the imaginary part of that  $\epsilon_i$  of silicon are expressed as

$$\epsilon_r = n_f^2 - \kappa_f^2 = \epsilon_{\text{Si}} \left( 1 - \frac{\omega_p^2 \tau^2}{1 + \omega^2 \tau^2} \right), \quad (1)$$

$$\epsilon_i = 2n_f \kappa_f = \epsilon_{\text{Si}} \frac{\omega_p^2 \tau}{\omega(1 + \omega^2 \tau^2)}, \quad (2)$$

where  $\omega$  is the angular frequency,  $\epsilon_{\text{Si}}$  is the dielectric constant of intrinsic silicon,  $n_f$  is the refractive index of silicon,  $\kappa_f$  is the extinction coefficient induced by the free carrier optical absorption,  $\omega_p$  is the plasma angular frequency, and  $\tau$  is the lifetime of carriers.  $\omega_p$  and  $\tau$  are expressed as

$$\omega_p = \sqrt{\frac{Ne^2}{m\epsilon_{\text{Si}}}}, \quad (3)$$

$$\tau = \frac{m\mu}{e}, \quad (4)$$

where  $N$  is the carrier density,  $e$  is the elemental charge,  $m$  is the effective mass of the carrier, and  $\mu$  is the carrier

mobility.  $\epsilon_r$  decreases because free carrier vibration occurs in the anti phase.  $\epsilon_i$  increases and absorption of the infrared light substantially occurs when many carriers respond.  $\epsilon_i$  is high for a low  $\omega$ . Therefore, the free carrier absorption is sensitively observed, especially for low wave numbers. The refractive index and extinction coefficient are respectively given as

$$n = \sqrt{\frac{\epsilon_r + \sqrt{\epsilon_r^2 + \epsilon_i^2}}{2\epsilon_0}}, \quad (5)$$

$$k = \frac{\epsilon_i}{\sqrt{2\epsilon_0\sqrt{\epsilon_r + \sqrt{\epsilon_r^2 + \epsilon_i^2}}}}, \quad (6)$$

where  $\epsilon_0$  is the dielectric constant in vacuum. Equations (5) and (6) show that the refractive index and extinction coefficient depend on the real and imaginary parts of the effective dielectric constant, respectively. They can be changed by existence of free carriers. Changes in  $n$  and  $k$  cause changes in the optical reflectivity and transmissivity of materials, respectively. The carrier density and carrier mobility can be determined by analysis of FTIR spectra with different angular frequencies.

Transmissivity spectra were calculated using calculated spectra (dashed curves) and using carrier density distribution obtained from as-implanted phosphorus concentration profile shown in Fig. 3 multiplied by the crystalline volume ratio shown in Fig. 5 for every laser irradiation condition, as shown in Fig. 8. Good agreements between the experimental and calculated spectra support the assumption of no carrier generation in amorphous regions. The free carrier distribution expanded to the surface region shown in Fig. 8(a) as the dwell time increased from 19 to 43  $\mu\text{s}$  in the case of 100 keV implantation. High activation in the region deeper than 130 nm was achieved for the dwell time of 25  $\mu\text{s}$  because of the complete recrystallization. On the other hand, the carrier density in the surface region was low because of the substantial amorphous phase.

In the cases of phosphorus implantations at 300 and 500 keV, the shape of the carrier density distribution was close to that of phosphorus concentration distributions for every laser irradiation case. These results indicate that the activation process was completed spatially uniformly in the case of phosphorus implantation at 300 and 500 keV. The implanted regions maintained their crystalline states. Thermal energy was only necessary to move phosphorus atoms located in interstitial sites into silicon lattice sites.

Figure 9 shows the sheet resistance and the total carrier density obtained by the free carrier absorption analysis as a function of the dwell time. The sheet resistance decreased from 1833, 497, and 295  $\Omega/\square$  to 141, 110, and 76  $\Omega/\square$  as the laser dwell time increased from 15 to 43  $\mu\text{s}$  for the implantations of 100, 300, and 500 keV, respectively, because of the increase in carrier density. The carrier densities for the case of 100 keV were lower than those of the cases of 300 and 500 keV for the short laser dwell time below 25  $\mu\text{s}$  because of the substantial amorphized region shown in Fig. 5. On the other hand, 43- $\mu\text{s}$  laser annealing achieved a carrier density of  $1.0 \times 10^{15} \text{ cm}^{-2}$  for every implantation condition. This indicates that phosphorus atoms were completely activated by the laser annealing.

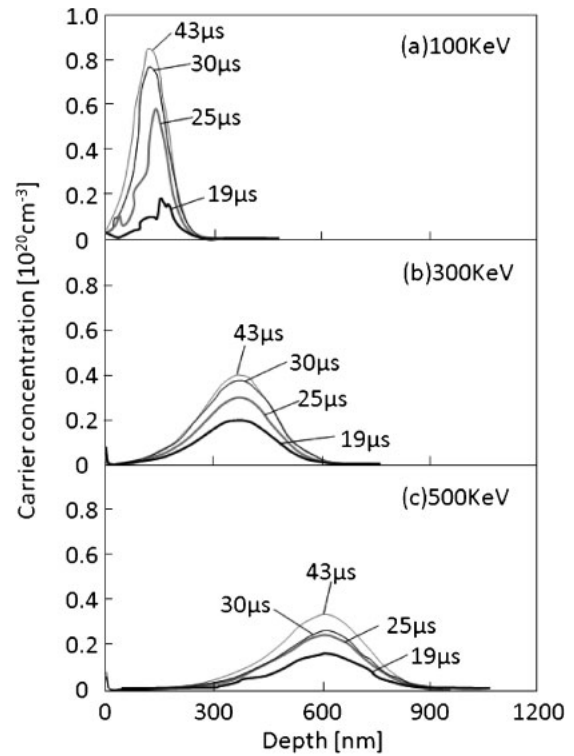


Fig. 8. Carrier density distribution obtained from the as-implanted phosphorus concentration profile shown in Fig. 3 multiplied by the crystalline volume ratio shown in Fig. 5 for every laser irradiation condition.

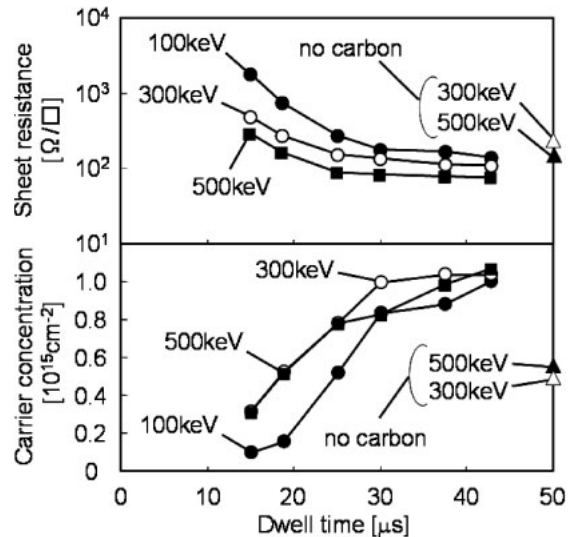


Fig. 9. Sheet resistance and total carrier density obtained by the free carrier absorption analysis in the cases of phosphorus implantations of 100, 300, and 500 keV as a function of dwell time. The sheet resistance and total carrier density in the case without carbon layer formation and with a laser dwell time of 50  $\mu\text{s}$  in the cases for phosphorus implantations of 300 and 500 keV are also plotted.

Figure 9 also shows the sheet resistance and the carrier density for phosphorus implanted samples at 300 and 500 keV and without carbon layer formation in the case of laser annealing with a dwell time of 50  $\mu\text{s}$ , for comparison of cases with carbon optical absorption layers. The sheet resistance and the carrier density were 230  $\Omega/\square$  and

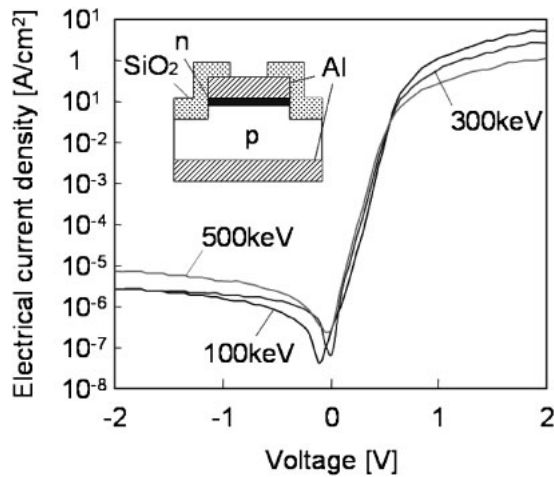


Fig. 10. *I*-*V* characteristics of laser annealed samples for phosphorus implantations at 100, 300, and 500 keV. The sample structure is represented in the inset.

$5.0 \times 10^{14} \text{ cm}^{-2}$  for implantation at 300 keV, respectively. These were  $143 \Omega/\square$  and  $5.5 \times 10^{14} \text{ cm}^{-2}$  for the case of 500 keV. Phosphorus activation was not effective compared with the cases with carbon optical absorption layers. In the case of phosphorus implantation at 100 keV, activation was not observed and the resistivity did not decrease with 50- $\mu\text{s}$  laser annealing without carbon layer. This is probably because insufficient thermal energy was provided to achieve recrystallization.

Figure 10 shows the *I*-*V* characteristics of the pn junction for the laser-annealed samples for phosphorus implantations at 100, 300, and 500 keV. Diodes with the mesa structure, as shown in the inset, were fabricated. The laser dwell time was 43  $\mu\text{s}$ . The diode factors were 1.58, 1.68, and 1.75 for bias voltages between 0.1 and 0.4 V for the cases of 100, 300, and 500 keV, respectively. The reverse bias currents at  $-2 \text{ V}$  were 2.7, 2.6, and 7.4  $\mu\text{A}/\text{cm}^2$  for the cases of 100, 300, and 500 keV implantation, respectively. This result reveals that phosphorus-doped regions were activated and the built-in-potential was well formed in the depletion regions underlying the top doped layers.

### 3.3 Boron doping

Figure 11 shows the boron atom in-depth profiles of the samples implanted with boron clusters at 6 keV with a boron atom concentration of  $1 \times 10^{15} \text{ cm}^{-2}$  and laser-annealed for a dwell time of 38  $\mu\text{s}$ . Boron atoms were concentrated at the surface region within a depth of 10 nm. The concentrations of boron incorporated in silicon were estimated as  $6.0 \times 10^{14}$  and  $3.3 \times 10^{14} \text{ cm}^{-2}$  for as-implanted and laser annealed samples, respectively. The SIMS measurements revealed that boron atoms did not diffuse into the silicon substrate by 38- $\mu\text{s}$  laser annealing, as shown in Fig. 11. They also revealed that the boron concentration in silicon was decreased after laser annealing. The top carbon layer might have absorbed boron atoms during laser heating because of stress at the carbon and silicon interface.

For samples implanted by boron-cluster implantation at 6 keV, decreases in transmissivity FITR spectra were observed when samples were annealed by laser for dwell times of 19 and 38  $\mu\text{s}$ . No valley or peak due to the optical

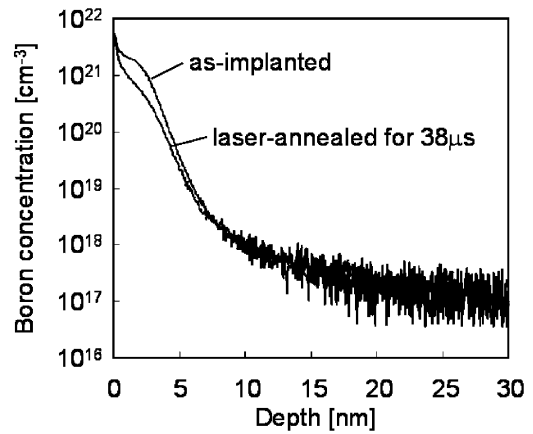


Fig. 11. Boron atom in-depth profiles of the as-implanted and laser-annealed samples for a dwell time of 38  $\mu\text{s}$  for an implantation of boron clusters when boron atoms at  $1.0 \times 10^{15} \text{ cm}^{-2}$  were implanted at 6 keV.

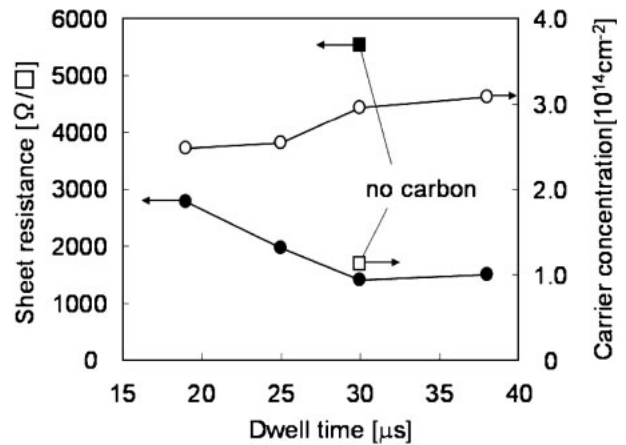
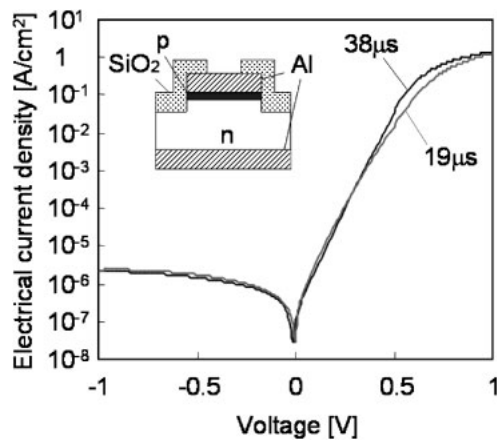


Fig. 12. Sheet resistance and total carrier density for the boron-doped sample obtained by the free carrier absorption analysis as a function of dwell time. The sheet resistance and total carrier density in the case without carbon layer formation and with a laser dwell time of 30  $\mu\text{s}$  are also plotted.

interference effect was observed in the spectra because the free carriers were concentrated in the shallow region. Figure 12 shows the sheet resistance and the total carrier density for the boron-doped sample obtained by free carrier absorption analysis as a function of dwell time. The sheet resistance decreased from 2502 to 1497  $\Omega/\square$  as the laser dwell time increased from 19 to 38  $\mu\text{s}$ . This was caused by an increase in the carrier density from  $2.5 \times 10^{14}$  to  $3.1 \times 10^{14} \text{ cm}^{-2}$ . The activation of dopant atoms was well achieved. The activation ratio for a dwell time of 38  $\mu\text{s}$  was estimated to be 0.92. The results of Figs. 11 and 12 revealed that the activation of impurities concentrated within the top 10 nm surface region was well achieved without the diffusion of impurities to the silicon substrate. The sheet resistance and the carrier density in the case without carbon layer formation and with a laser dwell time of 30  $\mu\text{s}$  are also shown in Fig. 12 for comparison with the case with carbon optical absorption layers. The sheet resistance and the carrier density were 5521  $\Omega/\square$  and  $1.1 \times 10^{14} \text{ cm}^{-2}$ , respectively. Although boron atoms were activated by the absorption of laser light in bulk silicon, the laser dwell time was



**Fig. 13.**  $I$ - $V$  characteristics for samples with boron implantation laser annealed for 19 and 38  $\mu\text{s}$ . The sample structure is represented in the inset.

insufficient because the heating power density was low owing to the low optical absorption coefficient.

Figure 13 shows pn diode characteristics with the mesa structure for the samples laser annealed for 19 and 38  $\mu\text{s}$  for the boron-cluster implanted samples. The diode factors were 1.80 and 1.57 for bias voltages between 0.1 and 0.4 V for the dwell times of 19 and 38  $\mu\text{s}$ , respectively. The reverse bias currents at  $-1$  V were 2.3 and 2.1  $\mu\text{A}/\text{cm}^2$  for the dwell times of 19 and 38  $\mu\text{s}$ , respectively. This result reveals that a heavily doped layer with a small depth was effectively activated using the present annealing method.

#### 4. Conclusions

We investigated the activation of silicon implanted with phosphorus and boron atoms using rapid CW infrared semiconductor laser annealing ranging from 15 to 43  $\mu\text{s}$ . We estimated the change in temperature on the silicon surface using a numerical analysis program constructed with the two-dimensional finite element method. The surface temperature increased to 1390  $^{\circ}\text{C}$  at maximum and the top 2  $\mu\text{m}$  surface region was heated above 1000  $^{\circ}\text{C}$  for longer than 22  $\mu\text{s}$  by irradiating the laser beam at 375  $\text{kW}/\text{cm}^2$  for 40  $\mu\text{s}$ . We carried out implantations of  $1 \times 10^{15} \text{ cm}^{-2}$  phosphorus atoms at 100, 300, and 500 keV for p-type silicon substrates, and boron clusters with a boron concentration of  $1 \times 10^{15} \text{ cm}^{-2}$  at 6 keV for n-type silicon substrates. 200-nm-thick carbon optical absorption layers were formed on the surface by sputtering. Laser irradiations with a laser power of 40 W and an effective heating intensity of 375  $\text{kW}/\text{cm}^2$  were conducted on the samples to activate impurity atoms. The phosphorus and boron atom in-depth concentration profiles were measured by SIMS. There was no change in the phosphorus concentration profile by laser annealing for every implantation case. Optical reflectivity spectra ranging from 250 to 1000 nm were measured to investigate the crystalline state in the surface region. The silicon surface region was amorphized by the phosphorus implantation at 100 keV. Laser annealing caused recrystallization in the

implanted region. On the other hand, the surface regions almost maintained their crystalline states in the cases of phosphorus implantations at 300 and 500 keV. FTIR transmissivity spectra were measured to analyze free carrier density in-depth profiles and sheet resistance using the free carrier absorption theory. Oscillation line shapes due to the optical interference effect were observed in the transmissivity spectra between 1000 and 7000  $\text{cm}^{-1}$  because free carriers were generated from phosphorus atoms implanted in the deep region from the surface. In the case of 100 keV implantation, the activation of phosphorus atoms proceeded according to the recrystallization process. On the other hand, the activation proceeded uniformly in the depth direction in the cases of 300 and 500 keV because the implanted regions almost maintained their crystalline states. The sheet resistance decreased to 141, 110, and 76  $\Omega/\square$  as the laser dwell time increased to 43  $\mu\text{s}$  for the implantations of 100, 300, and 500 keV, respectively, because of the increase in carrier density. Phosphorus atoms were almost completely activated in every implantation case by laser annealing for the dwell time of 43  $\mu\text{s}$ . The  $I$ - $V$  characteristics of the mesa structural diode fabricated with the samples for the implantations at 100, 300, and 500 keV revealed that the built-in potential was well formed in the depletion regions underlying the top doped layers. Boron atoms implanted in the shallow surface region were also well recrystallized and activated without diffusion into the silicon substrate by laser irradiation with a laser power of 375  $\text{kW}/\text{cm}^2$ . No valley or peak due to the optical interference effect was observed in the spectra because the free carriers were concentrated in the shallow region. The sheet resistance and total carrier density achieved were 1497  $\Omega/\square$  and  $3.1 \times 10^{14} \text{ cm}^{-2}$ , respectively, when the laser dwell time was 38  $\mu\text{s}$ . The activation ratio was estimated to be 0.92. The diode characteristics revealed that a heavily doped layer with a small depth was effectively activated by laser annealing.

- 1) M. Mehrotra, J. C. Hu, A. Jain, W. Shiao, V. Reddy, S. Aur, and M. Rodder: *IEDM Tech. Dig.*, 1999, p. 419.
- 2) T. Ito, K. Suguro, M. Tamura, T. Taniguchi, Y. Ushiku, T. Iinuma, T. Itani, M. Yoshioka, T. Owada, Y. Imaoka, H. Murayama, and T. Kusuda: *Ext. Abstr. 3rd Int. Workshop Junction Technology*, 2002, p. 23.
- 3) A. Shima and A. Hiraiwa: *Jpn. J. Appl. Phys.* **45** (2006) 5708.
- 4) K. Goto, T. Yamamoto, T. Kubo, M. Kase, Y. Wang, T. Lin, S. Talwar, and T. Sugii: *IEDM Tech. Dig.*, 1999, p. 931.
- 5) T. Sameshima, Y. Matsuda, Y. Andoh, and N. Sano: *Jpn. J. Appl. Phys.* **47** (2008) L1871.
- 6) N. Sano, N. Andoh, T. Sameshima, Y. Matsuda, and Y. Andoh: *Jpn. J. Appl. Phys.* **46** (2007) L620.
- 7) T. Sameshima, M. Maki, M. Takiuchi, N. Andoh, N. Sano, Y. Matsuda, and Y. Andoh: *Jpn. J. Appl. Phys.* **46** (2007) 6474.
- 8) T. Sameshima and N. Andoh: *Mater. Res. Soc. Symp. Proc.* **849** (2004) KK9.5.
- 9) K. Ukawa, Y. Sakakura, T. Sameshima, N. Sano, M. Naito, and N. Hamamoto: *Proc. Thin Film Materials and Devices Meet.*, 2008, p. 6-1.
- 10) K. Ukawa, T. Sameshima, N. Sano, M. Naito, and N. Hamamoto: *Proc. Workshop Active Matrix Flat Panel Displays*, Nara, 2009, p133.
- 11) S. Higashi and T. Sameshima: *Jpn. J. Appl. Phys.* **40** (2001) 480.
- 12) T. Sameshima, K. Ukawa, N. Sano, M. Naito, and N. Hamamoto: *Proc. Thin Film Materials and Devices Meet.*, 2009, p. 100228044.